Surface plasmon polariton propagation length: A direct comparison using photon scanning tunneling microscopy and attenuated total reflection

P. Dawson and B. A. F. Puygranier
Condensed Matter Physics and Materials Science Research Division, School of Maths and Physics, Queen's University of Belfast, Belfast BT7 1NN, United Kingdom

J-P. Goudonnet
Laboratorire de Physique de l'Université de Bourgogne, Equipe Optique Submicronique, Facultés Sciences Mirande, Boîte Postale 138, Université de Bourgogne, 21004 Dijon Cedex, France

(Received 24 July 2000; revised manuscript received 4 January 2001; published 25 April 2001)

The propagation of surface plasmon polaritons (SPP's) is studied using a photon scanning tunneling microscope (PSTM) and conventional attenuated total reflection (ATR). The PSTM experiment uses localized (focused beam) launching of SPP's at a wavelength of 632.8 nm. Propagation of the SPP is observed as an exponentially decaying tail beyond the launch site and the $1/e$ propagation length is measured directly for a series of Ag films of different thicknesses. The ATR measurements are used to characterize the thin film optical and thickness parameters, revealing, notably, the presence of a contaminating adlayer of Ag_2S of typical dielectric function, $8.7+i2.7$, and thickness 1–2 nm. Values of the SPP propagation length, based on the ATR-derived film parameters used in the four-media implicit SPP dispersion relation, show very good agreement with those based on the PSTM images for the case of undercoupled or optimally coupled SPP modes. The observed propagation lengths are quantitatively analyzed taking explicit account of additional intrinsic damping due to the growth of the Ag_2S layer and of reradiation of the SPP back into the prism outside the launch site. Finally, the PSTM images show excellent SPP beam confinement in the original propagation direction.

DOI: 10.1103/PhysRevB.63.205410 PACS number(s): 78.66.Bz, 71.36.+c

I. INTRODUCTION

Surface plasmon polaritons (SPP's) have been the subject of many experimental investigations using various techniques since the original theoretical description of ''lowered'' plasmon modes by Ritchie.[1] In this study we use the Kretschmann-Raether prism coupling technique[2] to excite SPP's and an optical scanning probe instrument to detect and monitor their propagation—the instrument used here is generally referred to as the photon scanning tunneling microscope (PSTM).[3] The aim is to elucidate and firmly connect the macro- and microscale optical characterization of SPP propagation. First, we place the current study in context by giving some background on the application of far-field and near-field optics in the excitation and detection of SPP modes.

A. Conventional or optical far-field techniques in the excitation and detection of SPP's

While the earliest work on plasmons was performed using excitation by electrons,[4] a theme carried forward in light emission from (i) metal-oxide-metal tunnel junctions[5–7] and (ii) the electron scanning tunneling microscope[8,9] (STM), the *optical* excitation of SPP's has proved to be more productive and accessible. The use of grating couplers[10] actually preceded the development of the prism coupling techniques of Otto[11] and of Kretschmann and Raether.[2] These techniques, used extensively in the study and application of SPP's,[12] provide matching of the parallel component of the wave vector of incident radiation to the real part of the SPP wave vector k_r:

$$k_r = \begin{cases} k_l n \sin\theta_{\mathrm{spp}} & \text{prism case} \quad (1a) \\ k_l \sin\theta_{\mathrm{spp}} + m k_g & \text{grating case,} \quad (1b) \end{cases}$$

where $k_l = \omega/c$ is the magnitude of the wave vector for light, θ_{SPP} is the angle of incidence for resonant coupling to the SPP mode, n is the prism refractive index [Eq. (1a)] and $k_g = 2\pi/\Delta$, where Δ is the grating period and m is an integer [Eq. (1b)].

B. Optical near-field techniques in the excitation and detection of SPP's

Early developments in the near-field excitation of surface electromagnetic modes were the edge launching and ''end-fire'' coupling techniques[13–15] used in the mid-ir spectral region. Some years later, in the visible region, an elegant scheme for *broadband* SPP excitation was introduced by Gruhlke and co-workers[16] and further investigated by Dawson, Bryan-Brown, and Sambles[17]—this relied on near-field fluorescent coupling of excited molecules with the SPP modes on an adjacent metal film. Edge launching and end-fire coupling may be regarded as one-dimensional precursors of point or tip launch schemes[18,19] in which light fed down an optical fiber, with a tip formed at its end, excites SPP's on a metal film held in the near-field of the tip. [Detection of SPP's occurs by virtue of radiative decay into the glass prism supporting the metal film in accordance with Eq. (1a), a process that is important in the analysis of the results presented in Sec. III.] The pertinent point is that sharp features (tips or edges), or indeed molecules, produce sufficiently large spatial Fourier field components in the near field to excite SPP

modes that characteristically have wave vectors larger than that of free electromagnetic radiation.

More commonly, scanning probe studies of plasmon resonances have used a probe or tip as a local detector, while the excitation process itself has been by means of a far-field optical input. The use of a *metallic* probe for localized interaction with an optically excited SPP mode was exploited in the scanning plasmon near-field microscope reported by Specht *et al.*,[20] a type of inverse arrangement of light emission from STM;[8,9] optical resolution of $\lambda/200$ was claimed. This scheme was further investigated by Kim *et al.*,[21] while a variant of the experiment, using atomic force microscopy (AFM) probing of SPP's has also been reported.[22] The STM was the first scanning probe instrument to be applied specifically[23,24] to the study of SPP propagation. The presence of the SPP is detected indirectly via additional contributions to the tunnel current due to thermal expansion effects as reported originally by Amer, Skumanich, and Ripple[25] and the rectification of the optical frequency ac field of the SPP that occurs on account of the nonlinear I-V characteristic of the STM tunnel junction.[26,27] Exploiting these effects Kroo *et al.*[23] and Thost *et al.*[24] measured SPP propagation lengths of 13.0 and 29.7 μm at $\lambda = 632.8$ nm on 40- and 55-nm-thick Ag films, respectively, and of 374 μm for a 30-nm-thick Au film at $\lambda = 2.64\ \mu$m.

Early work applying *optical* probes to SPP modes on metal films focused attention on the characterization and analysis of the enhanced electromagnetic fields associated with the excitations.[28,29] Subsequently, we exploited the PSTM in a focused-beam Kretschmann-Raether configuration to generate three-dimensional images of propagating SPP modes.[30–32] In addition to these basic propagation studies there has been particular interest and progress in the area of elastic scattering of SPP's from surface structures,[33–35] spawning the idea of the two-dimensional micro-optics of SPP's.[36] A fascinating branch of this field has been the study of multiple scattering and localisation of SPPs on rough metal films,[37] including those exhibiting fractal structure.[38]

There has been a parallel set of activities using scanning probe techniques in the excitation[39] and detection[40,41] of localized plasmon resonances on metallic nanoparticles. Observations have included a determination of the homogeneous line broadening of the plasmon resonance of a single nanoparticle[39] and a squeezing of the optical near field along a line of coupled nanoparticles.[41]

The object of the current investigation is to make a rigorous connection, on a sound physical basis, between the microscopic optical probe (PSTM) data on SPP propagation, and the macroscopic, far-field optical characterization yielded by ATR measurements. It is important, in our view, that the results of the scanning probe techniques do not exist in isolation. Although of a basic nature, this type of study is missing in the literature on the subject to date. The work that follows is essentially a quantitative development and analysis of the SPP propagation studies presented by us in Ref. 30.

II. EXPERIMENT

The samples in this study comprise thin Ag films deposited by thermal evaporation at a base pressure of $\leqslant 5 \times 10^{-5}$ Pa onto clean sections of silica slides (25×18 mm, approximately). These films readily formed a surface layer of silver sulfide, Ag_2S, hence the complete structures examined were of the form silica substrate/Ag/Ag_2S. The silica slides were coupled to silica prisms using index-matching gel in order to facilitate wave-vector matching between the incident light beams and the SPP mode at the Ag/Ag_2S/air interface. Sets of samples covering the thickness range 25–70 nm were prepared and examined. Here we report results on two such sets, series *A* and series *B*; within each series the samples are identified as $A1-A3$ and $B1-B3$, in order of decreasing thickness. A further sample, *C*, for which Ag_2S thickness was kept to a minimum, was examined. All measurements were taken in air.

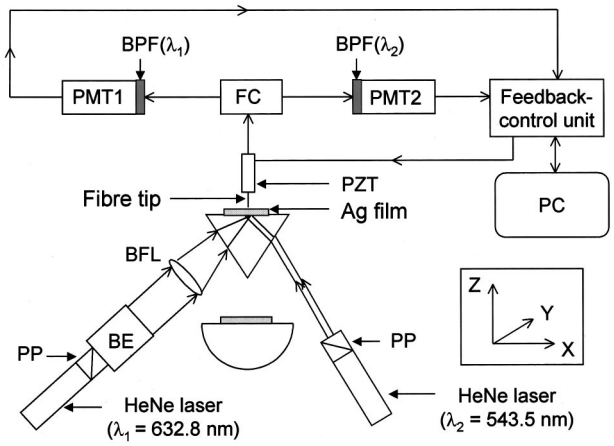

FIG. 1. Schematic diagram showing optical inputs to the PSTM. Sample comprises a Ag film deposited on silica slide interfaced to a coupling prism with index-matching gel. The beam from the red He-Ne laser, $\lambda_1 = 632.8$ nm, is first expanded, then focused to a tight spot centered on the SPP resonance angle to give localized launching of SPP's. The unfocused beam from the green He-Ne laser, $\lambda_2 = 543.5$ nm, incident at the SPP resonance angle for this wavelength, is used for the regulation of the tip-sample distance. The various system components are denoted by the following annotations: PP, prism polarizer; BE, beam expander; BFL, best-form laser lens; PZT, piezoelectric scanner tube; FC, 2×2 fiber coupler; BPF, optical bandpass filter; PMT, photomultiplier tube. The triangular section prism was used in case of series *B* (Fig. 5) and sample *C* (Fig. 6) and the semicylindrical prism in the case of series *A* (Fig. 3).

The PSTM arrangement is shown in Fig. 1. The important feature is that the tip-sample distance regulation is derived from an evanescent field at a different wavelength, λ_2, from that of the localized launch measurements. The λ_2 control beam is unfocused and thus covers a macroscopic area (~ 1 mm^2). On the bare coupling prism, without the sample in place, the control-beam evanescent field is that due to the total internal reflection of light incident at $\theta > \theta_c$. On the thin Ag films, the control beam is coupled to the SPP at the metal/air interface (at internal angle $\theta_{SPP} > \theta_c$) and the evanescent field is that associated with the SPP mode. Indeed, it is possible to set up the control-beam evanescent SPP field so that it extends across a metal film edge[32] or across a gentle step on a metal film[42] without significant radiative scattering,

for the purpose of studying the interaction of locally launched SPP's with such features.

The arrangement of a separate control beam means that the probe beam at λ_1 can be independent with respect to spatial extent, polarization, and time duration. In this experiment the red probe beam, of wavelength $\lambda_1 = 632.8\,\text{nm}$, is focused to a tight spot within the footprint of the green control beam of wavelength $\lambda_2 = 543.5\,\text{nm}$. The probe beam was first passed through a prism polarizer in order to select the *p*-polarized state and then expanded ($20\times$) prior to being focused, through the coupling prism, onto the Ag substrate surface using a best form laser lens of focal length 190 mm. This setup offers the necessary degree of probe beam confinement (on the order of 10 μm), along with a reasonable working distance between the bench optical components and the PSTM head. If a bare coupling prism of triangular section is used, the probe-beam evanescent field, as monitored by the PSTM, is well confined but of an elliptical footprint in the plane of the substrate;[30] the elliptical shape arises simply form the non-normal incidence of the input beam. If a semicylindrical coupling prism is used, there is additional focusing of the probe beam in one plane only. Thus, with the focusing optimized along the *X* direction (refer to Fig. 1), the evanescent field intensity is spread out in a long ridge in the *Y* direction.[31] A semicylindrical prism was used with the *A* series of samples, while triangular prisms were used with series *B* and sample *C*.

The signals at the two different wavelengths are independently detected using a (2×2) fiber coupler in conjunction with optical bandpass filters of appropriate center wavelengths. The fiber tips used in the experiment were directly etched on the input fibers of the coupler. The tips were bare, i.e., the sides were *not* coated with metal, the effective aperture being determined by the tip profile and the exponential decay of the electromagnetic field away from the sample surface. The PSTM images of SPP propagation are shown in Figs. 3, 5, and 6 (inset).

For ATR analysis the samples are mounted on triangular, silica coupling prisms, so that no beam focusing takes place at the input face and the angle of incidence remains well specified at the sample face. The ATR rig comprises two coaxially mounted, stepper-motor driven rotary tables, one supporting the sample and the other a Si photodiode that tracks and monitors the reflected beam. Prior to the sample the beam is split to yield an intensity reference signal that is divided into the reflected signal. Reference to total internal reflection on an uncoated section of the substrate establishes an absolute reflectance scale. Up to 1000 points per angle scan range are recorded. In their final form the data are presented as graphs of reflectance (corrected for reflections at the input and output faces of the prism) as a function of the internal angle of incidence in the prism (Figs. 2, 4, and 6).

The PSTM had only one rotary table incorporated in its design. This had two important consequences. First, detailed ATR measurements could not be made *in situ*, and so were performed in a separate system (described above) after completion of the PSTM measurements. The second was that only the control beam could be set up conveniently and rapidly in the PSTM. The more cumbersome optics associated with the focused probe beam had to be set up with some careful manipulation to ensure that it was incident at an angle centred at $\sim\theta_{\text{SPP}}$ and that it fell near the center of the $\sim$1-mm^2 footprint of the control beam. The setting-up procedure and the taking of results meant that a sample was in the PSTM for a period of typically several days to a week. The consequence of the delay between the PSTM and ATR measurements, in terms of sample aging, is given careful consideration, particularly in the case of series *B* where the delay was more protracted, 2–3 weeks. Series-*B* samples were examined first chronologically, prior to our realization of the degree of sample aging in the working environment.

The lateral (*X*-*Y*) calibration of the PSTM scanner tube is clearly very important. Since the PSTM setup had only optical feedback to regulate the tip-sample distance (i.e., there is no other distance regulation mechanism such as shear force), the calibration was carried out using a specially prepared glass substrate, patterned with an array of well-separated, square protrusions of side 1 μm and separation 8 μm. Although there is obviously some scattering of the evanescent field at the sides of the squares, the repeated optical pattern facilitated calibration of the lateral range to $\pm 2\%$ over the tube scanner range of 40 μm. The system software could compensate for nonlinearity in *X* and *Y* displacements and indeed also for *X*-*Y* cross-talk. Absolute calibration of the vertical movement is less important than the integrity of its linearity since only relative heights (intensities) are compared; the calibration was performed using both broad step features on a patterned glass substrate and an interferometric displacement technique.

There are two important points of a more general nature relating to the experiment:

(a) First, the PSTM makes use of a nonperturbative, bare optical fiber tip, as opposed to a metallic tip or metal-coated fiber tip. A variety of theoretical methods[43–45] concur to show that for a sharp (radius $<0.1\lambda$), uncoated, dielectric tip, the tip-sample coupling is negligible and the detected intensity is proportional to the squared modulus of the near field calculated at the position of the tip apex in the absence of the probe.

(b) Second, in the dual-beam PSTM technique that we have developed the signal indicating the presence of the SPP mode is generated *directly* through local scattering of the SPP evanescent field itself. There is an advantage here relative to STM measurements of SPP propagation,[23,24] which rely on second-order effects.[25–27] The technique is also more straightforward in principle than the far-field ATR study of the localized launching of SPP modes. In the ATR approach, both a directly reflected component of the stimulating light (the focused beam fills, or even overfills, the angular width of the SPP resonance centred at θ_{SPP}) and a component of light reradiated from the SPP mode propagating along the surface are necessarily detected.[46,47] Interference between the two components means that even simple information on propagation is not intuitively presented and must be deconvoluted from the reflected beam profile. An adjunct is that there is no real prospect of studying the full gamut of the SPP micro-optics in a tractable manner.

In summary, we emphasise the point that the crucial fea-

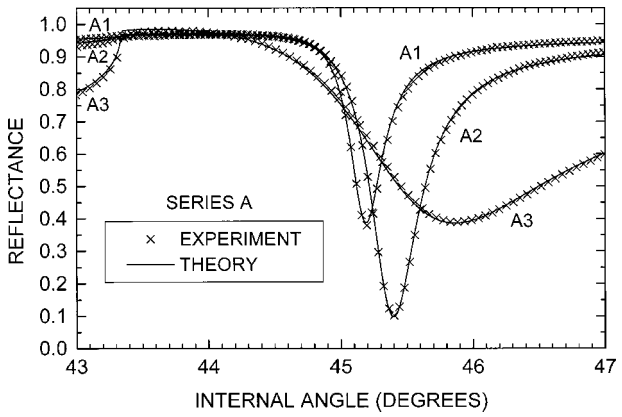

FIG. 2. ATR curves for series-*A* samples ($A1-A3$) taken using a silica coupling prism of equilateral triangular section. Crosses are experimental data and the solid line is the best-fit calculated curve in each case. Optical data derived from the fitting procedure are given in Table I.

ture concerning the PSTM measurements here is not subwavelength resolution, but the direct, relatively nonperturbative probing of the SPP evanescent field. This, combined with the *X*-*Y* scanning capability of the instrument, means that there is a graphic, three-dimensional representation of the SPP evanescent field intensity, rendering propagation away from the localized launch site directly observable in a very intuitive fashion.

III. RESULTS AND DISCUSSION

Figure 2 presents the ATR data for series *A*, while the PSTM images for samples $A1$ and $A3$ (longest and shortest propagation lengths, respectively) are shown in Fig. 3. Likewise the ATR data for series *B* and the PSTM images for samples $B1$ and $B3$ are shown in Figs. 4 and 5, respectively. In the PSTM images SPP propagation is clearly evidenced by the elongated tail section that decays exponentially away from the localized launch site. With regard to the ATR curves it is understood intuitively that the broader the SPP resonance, the more heavily damped the excitation and therefore the shorter its propagation length. This is graphically seen to be the case from a cross-comparison of the ATR curves and PSTM images.

A. Analysis of the ATR curves—optical and thickness data

From the ATR plots it can be seen that the range of Ag film thickness covered conditions ranging from undercoupling (samples $A1$, $B1$, and *C*) (Fig. 6) through optimum coupling (samples $A2$ and $B2$ approximate to this condition) to overcoupling (samples $A3$ and $B3$). With decreasing film thickness it is also seen that the reflectance for $\theta < \theta_c$ decreases, giving rise to a progressively more pronounced feature at θ_c.

Thin film optical and thickness data are generated by fitting calculated reflectance curves to the experimental data. This procedure is done with the aid of a minimization routine[48] with user-defined constraints on the data. In Figs. 2, 4, and 6, the experimental ATR data are depicted in the from

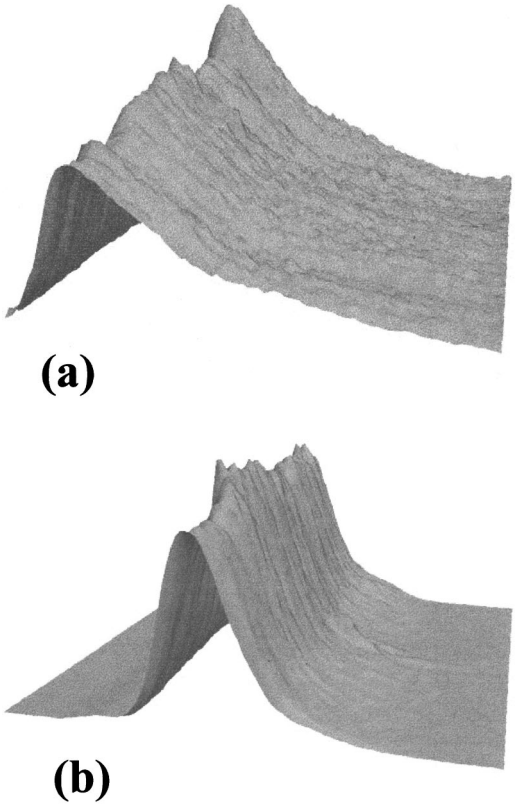

FIG. 3. PSTM images of SPP propagating (left to right) from localized launch site at $\lambda_1 = 632.8$ nm, the semicylindrical coupling prism used in the setup is shown in Fig. 1. The scan range is $36 \times 36\ \mu$m. (a) Sample $A1$; measured $1/e$ propagation length is 19.5 μm. (b) Sample $A3$; measured $1/e$ propagation length is 4.5 μm.

of crosses (every fifth point typically), while the best-fit computed curve is represented as a solid line. The data thus derived from the ATR curves are summarized in Table I, along with the propagation lengths, ${}^{\mathrm{ATR}}L_{\mathrm{SPP}}$, calculated on the basis of those data (as outlined in Sec. III B), and the lengths, ${}^{\mathrm{PSTM}}L_{\mathrm{SPP}}$, measured directly from the PSTM images.

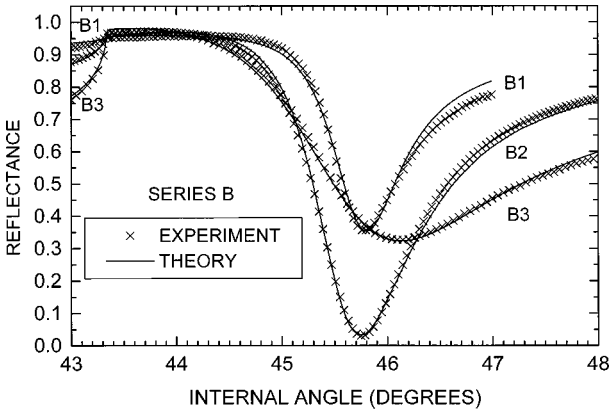

FIG. 4. ATR curves for series-*B* samples ($B1-B3$) taken using a silica coupling prism of equilateral triangular section. Crosses are experimental data and the solid line is the best-fit calculated curve in each case. Optical data derived from the fitting procedure are given in Table I.

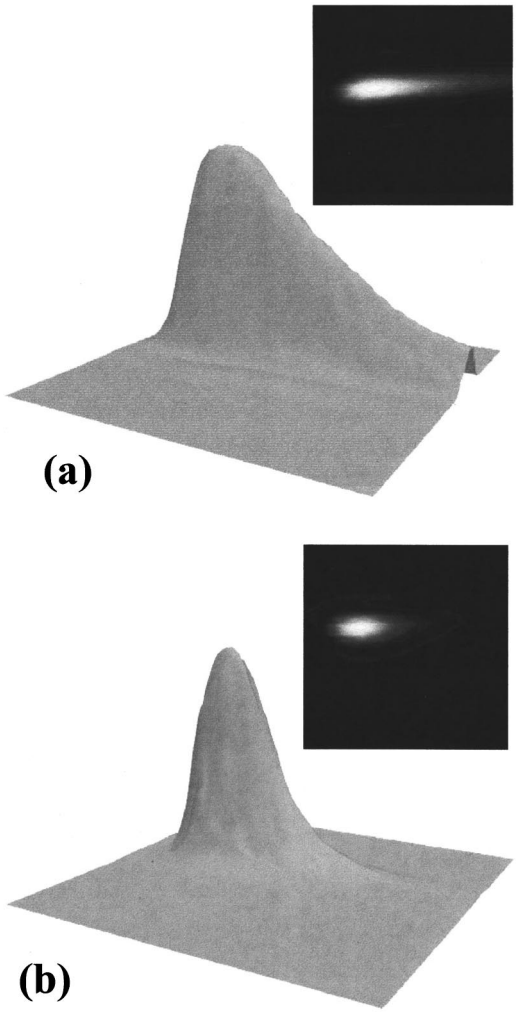

FIG. 5. PSTM images of SPP propagating (left to right) from a localized launch site at $\lambda_1 = 632.8$ nm, the triangular coupling prism used in the setup is shown in Fig. 1. The scan range is 36 $\times 36\ \mu$m and insets show two-dimensional views of images. (a) Sample $B1$; measured $1/e$ propagation length is 13.8 μm. (b) Sample $B3$; measured $1/e$ propagation length is 4.9 μm.

Before addressing the comparison of the differently derived propagation lengths, it is necessary to consider the ATR-based optical dielectric function and thickness data. The first important point is that the inclusion of a Ag_2S surface layer is found to be essential; the thin-film system is thus modeled as a four-media, three-interface, silica/Ag/Ag_2S/air structure. (The growth of Ag_2S is not surprising, since the laboratory was situated in the vicinity of a coal-burning plant.) In all cases the optical data for Ag was tightly constrained in the fitting procedure, taking as guidance the typical values cited in the literature;[49–51] the film thickness was loosely constrained. Extant data for the Ag_2S dielectric function[52–55] display a real part in the range 5.8–9.0 and an imaginary part that varies from 1.8 to 6.7 at $\lambda = 632.8$ nm. Several investigations have addressed SPP monitoring of Ag_2S growth,[54,56,57] with Wilson[54] producing $\varepsilon_{Ag_2S} = 7.34 + i6.70$, while others[56,57] have actually utilized the long-standing ellipsometric data of Bennett and co-workers[52]

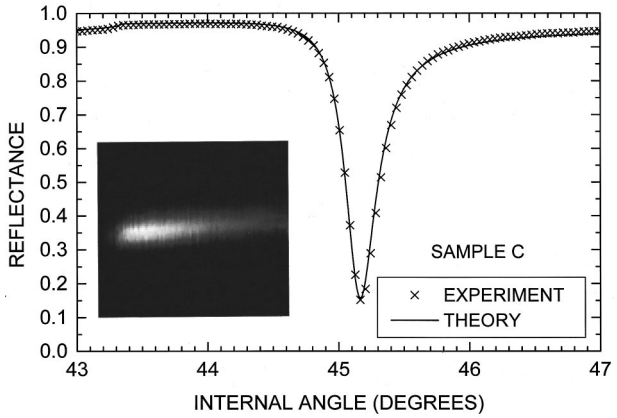

FIG. 6. ATR curve for sample C taken using a silica coupling prism of equilateral triangular section. Crosses are experimental data and the solid line is the best-fit calculated curve. Optical data derived from the fitting procedure are given in Table I. The inset shows a two-dimensional PSTM image of SPP propagation; the scan range is $40 \times 40\ \mu$m.

($\varepsilon_{Ag_2S} = 8.5 + i2.0$). In view of such variation, the optical data for the Ag_2S ''adlayer'' were loosely constrained in our semiautomatic fitting procedure (value ranges of 5–10 and 0–5 for the real and imaginary parts of ε_{Ag_2S}, respectively), as was the thickness. The fitting procedure yielded an average value of $\varepsilon_{Ag_2S} = 8.69 + i2.72$ across all samples, except $B1$. Sample $B1$ was the most awkward to fit and produced a value of $\varepsilon_{Ag_2S} = 9.86 + i4.50$, out of line with those of the other samples (see Table I). Series B samples are generally more contaminated than series A samples (average value of $t_{Ag_2S} = 2.06$ nm as opposed to 1.27 nm), while sample C ($t_{Ag_2S} = 0.85$ nm) is the least contaminated, as intended. In addition, in series B, the magnitude of ε_r for the Ag film itself is less than for series A and sample C, while ε_i assumes a greater value. This indicates a possible degradation of the Ag film itself as the sulfide ingresses along Ag grain boundaries.[53,58]

B. Determination of propagation lengths

1. PSTM data

In the PSTM images the $1/e$ propagation length for SPP's, ${}^{PSTM}L_{SPP}$, may be measured directly from the exponentially decaying tail outside the launch site. For each image, several line scans in the exponential tail section are extracted. A simple exponential decay curve is fitted to each set of data [as were straight lines to the corresponding ln (intensity) plots]. The quality of the individual fits is generally very good with a variance in the range 0.01–0.1. The small variation in ${}^{PSTM}L_{SPP}$ between different line sections taken from the same image appears random in nature and is not, for example, related to the launch intensity. The variation gives rise to estimated errors of between $\pm 2.5\%$ for the longer propagation lengths (14–20 μm) and $\pm 5\%$ for the shorter propagation lengths ($\sim 5\ \mu$m).

TABLE I. Summary of ATR and PSTM data. The thin-film optical (dielectric function) and thickness data for the Ag film and Ag_2S adlayer are based on optimized fits of calculated to experimental ATR curves (Figs. 2, 4, and 6). The 1/*e* SPP propagation length calculated on the basis of the ATR thin-film parameters (as described in the text) is denoted ${}^{\mathrm{ATR}}L_{\mathrm{SPP}}$, while that observed directly in the PSTM images is denoted ${}^{\mathrm{PSTM}}L_{\mathrm{SPP}}$.

	Optical and thickness data determined from ATR				SPP 1/*e* propagation length calculated from ATR data	SPP 1/*e* propagation length measured from PSTM data
Sample	$\varepsilon_{\mathrm{Ag}}$	t_{Ag} (nm)	$\varepsilon_{\mathrm{Ag_2S}}$	$t_{\mathrm{Ag_2S}}$ (nm)	${}^{\mathrm{ATR}}L_{\mathrm{SPP}}$ (μm)	${}^{\mathrm{PSTM}}L_{\mathrm{SPP}}$ (μm)
*A*1	$-17.93+i0.79$	61.6	$8.71+i2.98$	1.17	19.3	19.5
*A*2	$-17.18+i0.74$	52.6	$8.92+i2.57$	1.57	13.7	13.6
*A*3	$-16.99+i0.79$	27.1	$8.64+i2.69$	1.07	3.2	4.5
*B*1	$-16.54+i0.95$	55.0	$9.86+i4.50$	2.65	7.5	13.8
*B*2	$-16.69+i0.94$	37.2	$8.63+i2.82$	2.02	4.0	7.8
*B*3	$-16.62+i0.94$	25.9	$8.19+i3.11$	1.52	2.2	4.9
*C*1	$-17.65+i0.73$	57.0	$9.03+i2.17$	0.85	20.7	18.8

2. ATR data

The values of ${}^{\mathrm{PSTM}}L_{\mathrm{SPP}}$ may then be compared with values based on the ATR measurements, ${}^{\mathrm{ATR}}L_{\mathrm{SPP}}$, that are derived as follows. The optical and thickness data arising from the fitting procedure on the ATR curves (Sec. III A) are input to a program to calculate the SPP dispersion and damping properties. The program is based on the well-known SPP multilayer damping/dispersion relations.[59] These equations are set up such that a driving field is not included, that is to say the normal modes of the thin-film system are calculated. The calculation is thus pertinent to the region outside the launch site in the PSTM experiments—that is why care is taken to derive values of ${}^{\mathrm{PSTM}}L_{\mathrm{SPP}}$ from only the decaying tail section outside the launch region in the PSTM images. The dispersion/damping relation relevant to the samples examined here is that for a four-media, three-interface system, which accommodates the presence of the thin contaminating layer of Ag_2S on the surface of the Ag film,

$$\begin{vmatrix} 1 & -1 & -1 & 0 & 0 & 0 \\ \frac{\varepsilon_0}{k_0} & -\frac{\varepsilon_1}{k_1} & \frac{\varepsilon_1}{k_1} & 0 & 0 & 0 \\ 0 & e^{k_1 d_1} & e^{-k_1 d_1} & -1 & -1 & 0 \\ 0 & \frac{\varepsilon_1}{k_1} e^{k_1 d_1} & -\frac{\varepsilon_1}{k_1} e^{-k_1 d_1} & -\frac{\varepsilon_2}{k_2} & \frac{\varepsilon_2}{k_2} & 0 \\ 0 & 0 & 0 & e^{k_2 d_2} & e^{-k_2 d_2} & -1 \\ 0 & 0 & 0 & \frac{\varepsilon_2}{k_2} e^{k_2 d_2} & -\frac{\varepsilon_2}{k_2} e^{-k_2 d_2} & \frac{\varepsilon_3}{k_3} \end{vmatrix} = 0. \tag{2}$$

Further details on the calculation are given by Connolly and Dawson.[60] The program yields a value of $k_{\mathrm{SPP}}=k_r+ik_i$, where k_r and k_i are the real and imaginary parts of the SPP wave vector, determining the dispersion and damping of the mode, respectively. (Propagation in the *X* direction is assumed—see Fig. 1—and no explicit vector notation is therefore used.) The 1/*e* propagation length is related to the damping term through ${}^{\mathrm{ATR}}L_{\mathrm{SPP}}=1/(2k_i)$.

C. Analysis of propagation lengths

1. Series A and sample C

Examining the propagation lengths (Table I), it is clear that there is good agreement between those calculated from the ATR curves, ${}^{\mathrm{ATR}}L_{\mathrm{SPP}}$, and those extracted from the PSTM images, ${}^{\mathrm{PSTM}}L_{\mathrm{SPP}}$, for the case of samples *A*1, *A*2, and *C*. The agreement is less good for sample *A*3, while for

TABLE II. SPP propagation lengths, calculated on the basis of the optical data yielded by analysis of the ATR curves for samples $A1-A3$ and C. Sample labels and thicknesses of Ag and Ag_2S layers are given in columns 1 and 2, respectively. For each sample the propagation length is calculated for the actual film structure ($^{ATR}L_{SPP}$, column 6—as in Table I) and for three other notional cases using the optical properties specified in Table I: (a) Ag of semi-infinite optical thickness (taken as 200 nm) with no Ag_2S overlayer (column 3); (b) Ag of the characterized film thickness with no Ag_2S overlayer (column 4); and (c) Ag of semi-infinite optical thickness with a Ag_2S overlayer of characterized film thickness (column 5). The values of ΔL specify the decrease in propagation length due to reradiation losses (columns 7 and 10) and to intrinsic damping by addition of the Ag_2S layer (columns 8 and 9) in proceeding from the optimum length, $L_{Ag(\infty)}$, [SPP on optically thick, clean Ag (column 3)] to that for the actual Ag/Ag_2S film structure via two different pathways.

1	2	3	4	5	6	7	8	9	10
Sample	t_{Ag} and t_{Ag_2S} (nm)	$L_{Ag(\infty)}$ (μm)	$L_{Ag(t)}$ (μm)	$L_{Ag(\infty)/Ag_2S}$ (μm)	$^{ATR}L_{SPP}$ $Ag(t)/Ag_2S$ (μm)	ΔL $Ag_\infty \rightarrow Ag_t$ reradiation loss (μm)	ΔL $Ag_\infty \rightarrow Ag_t + Ag_2S$ Ag_2S loss (μm)	ΔL $Ag_\infty \rightarrow Ag_\infty + Ag_2S$ Ag_2S loss (μm)	ΔL $Ag_\infty \rightarrow Ag_t + Ag_2S$ reradiation loss (μm)
$A1$	61.6 1.17	37.7	29.0	23.2	19.3	−8.7	−9.7	−14.5	−3.9
$A2$	52.6 1.57	36.8	20.8	20.3	13.7	−16.0	−7.1	−16.5	−6.6
$A3$	27.1 1.07	33.7	3.7	22.3	3.2	−30.0	−0.5	−11.4	−19.1
C	57.0 0.85	39.4	26.2	28.9	20.7	−13.2	−5.5	−10.5	−8.2

samples $B1-B3$ the value of $^{PSTM}L_{SPP}$ is approximately double that of $^{ATR}L_{SPP}$. To aid the discussion on the factors that influence the propagation length, Table II is presented, in which values of propagation length are calculated for various scenarios (series A and sample C only). These consist of an ideal semi-infinite Ag/air system in which there is no contaminating Ag_2S layer and examples of thin-film structures intermediate between the ideal case and the samples actually observed. The value of $L_{Ag(\infty)}$ cited for the semi-infinite Ag/air case is based on the actual Ag optical data as derived from the ATR measurements for the particular sample concerned. This may be regarded as the maximum achievable propagation length on the material of that sample. It can be seen from Table II that $L_{Ag(\infty)}$ is actually quite sensitively dependent on the value of ε_{Ag}.

The fact that $^{PSTM}L_{SPP}$ is significantly less than $L_{Ag(\infty)}$ requires consideration of several important issues.

(a) The first pertinent issue is the influence of the Ag_2S layer. The fact that a polarizable medium is adjacent to the interface supporting the SPP leads to a redistribution of the mode electromagnetic energy such that damping in the metallic substrate actually increases, leading to shorter propagation lengths. The effect is well documented in the literature[12] and is the basis for SPP sensors of various types. Equally importantly here, however, the Ag_2S layer has a significant value of the imaginary part of its dielectric function. It is thus an optically ''lossy'' medium and is responsible for significant internal damping of the SPP energy. Considering the data for sample $A1$ in Table II, it can be seen that the ideal-case propagation length, $L_{Ag(\infty)}=37.7\,\mu$m, is reduced to 23.2 μm by the addition of just 1.17 nm of Ag_2S of dielectric function $\varepsilon_{Ag_2S}=8.71+i2.98$. Similarly, if we start from a clean Ag film of the actual thickness of the sample and add the Ag_2S layer the propagation length reduces from 29.0 to 19.3 μm.

(b) The second consideration is reradiation of the locally launched SPP mode that occurs in the PSTM setup. As the SPP propagates along the surface of the Ag film (outside the launch site) it can couple back to radiation in the silica substrate. This constitutes a loss of energy from the mode and thus decreases the propagation length. This loss mechanism is necessarily always present since there must be finite coupling, across the metal film, between free electromagnetic radiation in the substrate and the SPP mode on the outer surface of the sample in order to excite the mode in the first place. The magnitude of the reradiation is simply a function of the thickness of the film supporting the SPP mode and may be assessed from the data in Table II. For sample $A1$, for example, the reradiation loss accounts for a reduction in propagation length by 8.7 μm from $L_{Ag(\infty)}=37.7\,\mu$m for clean, semi-infinite Ag to 29.0 μm on a clean Ag film of thickness, 61.6 nm.

An examination of Table II shows clearly that it is not feasible to identify separately the loss in propagation length (relative to the ideal case) due to surface contamination and radiative damping. The two loss mechanisms are interrelated and it is a matter of choice how one notionally progresses from the ideal system with $L_{Ag(\infty)}$ to the experimental system with $^{PSTM}L_{SPP}$. However, it is clear that both damping mechanisms play comparably large roles.

(c) The third important point relates to the calculation of the SPP damping (and dispersion) that is crucial to the analysis of our measurements since it makes the link between the data obtained under the condition of a driving field being present (ATR case) and where such a field is absent (PSTM case, outside the localized launch site). We comment on the

solution of the SPP dispersion relation for a thin-film system with reference to the work of Wendler and Haupt,[61] who present two ''virtual mode'' SPP solutions. Their type I solution corresponds to a pole in the reflectance of the standard Fresnel reflectance function, where the denominator apparently goes to zero. Physically this situation corresponds to no driving field being present and is taken to represent free SPP propagation. Equation (2) expresses this condition for the four-media, three-interface case. Type II solutions, in the terminology of Ref. 61 correspond to the case of a zero in the numerator of the reflectance function—here there is a driving field, but no reflected field and this condition is taken to offer an accurate description of the data obtained in ATR experiments. Unfortunately in Ref. 61 it was found that the value of k_i became negative for small coupling gaps (i.e., the thickness of the metal film itself in the Kretschmann-Raether configuration), implying an unphysical SPP energy amplification process. Mathematically we find that this behavior is allowable but we constrain the damping term to increase with decreasing thickness. Thus the difference between the value of k_i for the case of a semi-infinite metal and the larger k_i value at finite thickness is taken to represent damping due to reradiation into the substrate. This leads to a satisfactory situation physically. For example, at the thickness for optimum coupling in the ATR geometry, t_{opt}, the radiative and internal damping components are exactly equal. (At this point the Haupt and Wendler value of k_i passes through zero.) Conversely, in terms of free SPP propagation on a film of thickness, t_{opt}, the mode has a propagation length exactly one-half of that which it attains on the surface of a semi-infinite sample for which the radiative damping term is zero.

Our procedure works well for films in the thickness range from semi-infinite (taken here as 200 nm) to slightly less than t_{opt}. However, for films of thickness significantly less than t_{opt}, (overcoupled ATR regime) the damping appears to run off rapidly leading to shorter values of ${}^{\mathrm{ATR}}L_{\mathrm{SPP}}$ than should be the case. (The computer routine can also become unstable for very thin films, generating spurious values for k_r and k_i.) We consider this to be the primary reason for the disagreement between the calculated value of ${}^{\mathrm{ATR}}L_{\mathrm{SPP}}$ and ${}^{\mathrm{PSTM}}L_{\mathrm{SPP}}$ in the case of sample $A3$.

Finally in relation to point (c) it is important to note also the recent work of Van Labeke, Baida, and Vigoureux[62] and Baida, Van Labeke, and Vigoureux,[63,64] which replicates very well the type of results (i.e., PSTM images) presented here and in our previous PSTM work on SPP's.[30–32] In those articles the full three-dimensional (3D) Gaussian nature of the input beam is rigorously taken into account, as are the detailed launching conditions and the subsequent SPP propagation. For a set of conditions that mimic the experimental ones reported in Ref. 30 (i.e. Gaussian beam of width 7.9 μm, $t_{\mathrm{Ag}}=53$ nm, $\varepsilon_{\mathrm{Ag}}=-17.9+i0.7$) Baida, Van Labeke, and Vigoureaux[63] find ${}^{\mathrm{theory}}L_{\mathrm{SPP}}=22.5\,\mu$m. There are two important points of comparison in relation to this value. First, it was remarked[63] that it can be compared to a theoretical limit of 24.3 μm. The latter figure refers to the case of the Ag film as outlined above, but for the case of infinite plane-wave SPP propagation, the assumption that underpins the analysis performed here. In other words, the application of Eq. (2) will lead to a small overestimation of the value of ${}^{\mathrm{ATR}}L_{\mathrm{SPP}}$, compared with the theory developed by Baida, Van Labeke, and Vigoureaux[63] Second, comparison was made with the significantly smaller value of ${}^{\mathrm{PSTM}}L_{\mathrm{SPP}}=13.7\,\mu$m found experimentally.[30] The authors surmised correctly that the condition of the metal surface is responsible for the large discrepancy. Following the analysis pertaining to Eq. (2) here, we may retrospectively add a layer of Ag_2S with $\varepsilon_{\mathrm{Ag_2S}}=8.69+i2.72$, $t_{\mathrm{Ag_2S}}=1.27$ nm (averaged data for series A here) to the Ag film of Ref. 30, but using the actual Ag data derived here for the series-A samples ($\varepsilon_{\mathrm{Ag}}=-17.37+i0.77$). This procedure modifies the calculated propagation length, ${}^{\mathrm{ATR}}L_{\mathrm{SPP}}$, from 24.3 to 22.0 μm for the clean Ag film and decreases it to 14.9 μm for the Ag_2S-contaminated film. The significant discrepancy between the experimental value of Ref. 30 and that found by Baida, Van Labeke, and Vigoureux[63] is thus largely resolved.

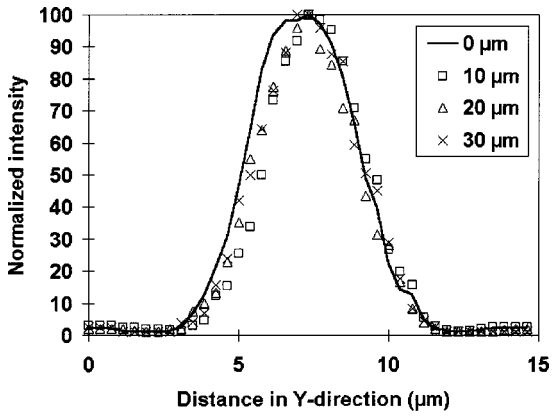

FIG. 7. Cross sections of the PSTM image of Fig. 5(a) of SPP propagating on sample $B1$, taken normal to the direction of propagation at various distances along the SPP path: —, center of launch site; □, ~10 μm; △, ~20 μm; and ×, ~30 μm from the center of the launch site. Sections are normalized to same maximum intensity value.

2. Series B

The comments in relation to sample $A3$ with regard to underestimation of ${}^{\mathrm{ATR}}L_{\mathrm{SPP}}$, apply to samples $B3$ and $B2$ (slightly overcoupled) to some extent also. However, in the case of the series-B samples, the overriding reason for the disagreement between ${}^{\mathrm{PSTM}}L_{\mathrm{SPP}}$ and ${}^{\mathrm{ATR}}L_{\mathrm{SPP}}$ is due to a real physical effect, the aging of the samples by the growth of further Ag_2S between the PSTM and ATR measurements. To demonstrate the point, if the Ag_2S layer, as characterized on sample $B1$, is replaced by a layer of the average dielectric and thickness data for the series-A samples ($\varepsilon_{\mathrm{Ag_2S}}=8.69+i2.72$, $t_{\mathrm{Ag_2S}}=1.27$) then the value of ${}^{\mathrm{ATR}}L_{\mathrm{SPP}}$ increases from 7.5 to 12.7 μm, in much better agreement with the value of ${}^{\mathrm{PSTM}}L_{\mathrm{SPP}}=13.8\,\mu$m.

Finally, we consider Fig. 7 and the SPP behavior in the Y direction, i.e., normal to the propagation direction. The figure shows sections of the evanescent field intensity for sample $B1$ as monitored by the PSTM in the Y direction. The four cross sections [derived from the image of Fig. 5(a)] were

taken at approximately 10-μm intervals along the propagation path with the first section being taken across the center of the launch site; the line profiles are all normalized to the same maximum value. Figure 7 illustrates that, even on a Ag_2S-contaminated surface, the SPP remains extremely well confined in the original launch direction. The high degree of confinement in propagation is confirmed from samples $B2$ and C, but sample $B3$ displays rather too short a propagation length to make any such measurements very meaningful. It may be concluded that there is no significant elastic SPP→SPP scattering that is strongly directional; significant forward scattering, for example, would lead to a broadening of the successive profiles in Fig. 7. However, an angularly isotropic scattering (detectable outside the specular beam reflection in ATR measurements) would give rise to a small background intensity outside the main SPP beam and may not be readily detectable in the PSTM images.

IV. SUMMARY AND CONCLUSIONS

This investigation was confined to the issue of SPP propagation. Without a proper understanding of this most basic of physical properties and ultimately of the optimization of ${}^{\mathrm{PSTM}}L_{\mathrm{SPP}}$, the prospects for multicomponent manipulation of SPP's and hence SPP micro-optics are very limited. Indeed, it may not be possible to properly understand and interpret images of the SPP interaction with even single surface features. For example, in a further study[42] in which we address SPP propagation over a gentle Ag step structure, it is clearly important to characterize the propagation on the thinner and thicker plane film regions either side of the step, in order to ascertain SPP properties across the step. On the other hand, the SPP ''flashlights'' reported in Ref. 34 constitute, we believe, a case of image misinterpretation. The authors claim the flashlights arise from the launching of propagating SPP's from asperities on the surface of a metal film. However, the cited propagation lengths from adjacent features on the same, 80-nm-thick Ag film range from 7 to 30 μm. For a clean, 80-nm-thick Ag film the SPP propagation length is 37.0 μm (using our best case, sample C data, $\varepsilon_{\mathrm{Ag}}=-17.65+i0.73$); to obtain propagation lengths of 30 and 7 μm would, for example, require the presence of 0.50 and 5.5 nm of Ag_2S, respectively, based on our average Ag_2S data, $\varepsilon_{\mathrm{Ag_2S}}=8.69+i2.72$. We do not consider such variation in the Ag_2S thickness on immediately adjacent regions of the same Ag film to be physically reasonable.

In summary, this investigation has demonstrated the connection between conventional, macroscopic characterization of SPP's using ATR and SPP propagation properties as determined from PSTM measurements. In the undercoupled to optimally coupled regime (thicker Ag films) good agreement has been achieved on the SPP propagation lengths derived from the two types of measurements. The analysis highlights limitations on the propagation length due to enhanced intrinsic energy dissipation from Ag_2S growth and reradiation of the SPP back into the prism. In addition, it was observed from the PSTM images that even for these contaminated Ag samples, excellent directionality of the SPP propagation away from the launch site is preserved.

ACKNOWLEDGMENTS

We would like to acknowledge the financial support of the CNRS and the Royal Society under the European Science Exchange Program to facilitate the inception of this work, which is currently supported by the U.K. Engineering and Physical Sciences Research Council under Grant No. GR/L31937. B.A.F.P. would like to thank the European Social Fund and Queen's University, Belfast for financial support. In addition, we are very grateful for the excellent technical support offered by Yvon Lacroute, Christof Aquilina, and Terry McKenna.

[1] R. H. Ritchie, Phys. Rev. **106**, 874 (1957).
[2] E. Kretschmann and H. Raether, Z. Naturforsch. A **23**, 2135 (1968).
[3] R. C. Reddick, R. J. Warmack, and T. L. Ferrell, Phys. Rev. B **39**, 767 (1989).
[4] H. Raether, Surf. Sci. **8**, 233 (1967).
[5] T.-L. Hwang, S. E. Schwarz, and R. K. Jain, Phys. Rev. Lett. **36**, 379 (1976).
[6] J. Lambe and S. L. McCarthy, Phys. Rev. Lett. **37**, 923 (1976).
[7] J. R. Kirtley, T. N. Theis, J. C. Tsang, and D. J. DiMaria, Phys. Rev. B **27**, 4601 (1983); P. Dawson, D. G. Walmsley, H. F. Quinn, and A. J. L. Ferguson, *ibid.* **30**, 3164 (1984); M. Hänisch and A. Otto, J. Phys.: Condens. Matter **6**, 9659 (1994).
[8] J. K. Gimzewski, B. Reihl, J. H. Coombs, and R. R. Schlitter, Z. Phys. B: Condens. Matter **72**, 497 (1988).
[9] R. Berndt, in *Scanning Probe Microscopy, Analytical Methods*, edited by R. Wiesendanger (Springer, Berlin, 1998), Chap. 5, p. 97.
[10] Y.-Y. Teng and E. A. Stern, Phys. Rev. Lett. **19**, 511 (1967).
[11] A. Otto, Z. Phys. **216**, 398 (1968); A. Otto, Phys. Status Solidi **26**, K99 (1968).
[12] H. Raether, in *Physics of Thin Films*, edited by G. Hass, M. H. Francombe, and R. W. Hoffman (Academic, New York, 1977), Vol. 9, p. 145.
[13] J. Schoenwald, E. Burstein, and J. M. Elson, Solid State Commun. **12**, 185 (1973).
[14] K. Bhasin, D. Bryan, R. W. Alexander, and R. J. Bell, J. Chem. Phys. **64**, 5019 (1976).
[15] Y. J. Chabal and A. J. Sievers, Appl. Phys. Lett. **32**, 90 (1978).
[16] R. W. Gruhlke, W. R. Holland, and D. G. Hall, Phys. Rev. Lett. **56**, 2838 (1986); R. W. Gruhlke and D. G. Hall, Appl. Phys. Lett. **53**, 1041 (1988).
[17] P. Dawson, G. Bryan-Brown, and J. R. Sambles, J. Mod. Opt. **41**, 1279 (1994).
[18] B. Hecht, H. Heinzelmann, and D. W. Pohl, Ultramicroscopy **57**, 228 (1995); B. Hecht, H. Bielefeld, L. Novotny, Y. Inouye, and D. W. Pohl, Phys. Rev. Lett. **77**, 1889 (1996).
[19] L. Novotny, B. Hecht, and D. W. Pohl, J. Appl. Phys. **81**, 1798 (1997).

[20] M. Specht, J. D. Pedarnig, W. M. Heckl, and T. W. Hansch, Phys. Rev. Lett. **68**, 476 (1992).
[21] Y. K. Kim, P. M. Lundquist, J. A. Helfrich, J. M. Mikrut, G. K. Wong, P. W. Auvil, and J. B. Ketterson, Appl. Phys. Lett. **66**, 3407 (1995).
[22] R. G. B. de Hollander, N. F. Van Hulst, and R. P. H. Kooyman, Ultramicroscopy **57**, 263 (1995).
[23] N. Kroo, J.-P. Thost, M. Völcker, W. Krieger, and H. Walther, Europhys. Lett. **15**, 289 (1991).
[24] J.-P. Thost, W. Krieger, N. Kroo, Z. Szentirmay, and H. Walther, Opt. Commun. **103**, 194 (1993).
[25] N. M. Amer, A. Skumanich, and D. Ripple, Appl. Phys. Lett. **49**, 137 (1986).
[26] P. H. Cutler, T. E. Feuchtwang, T. T. Tsong, H. Nguyen, and A. A. Lucas, Phys. Rev. B **35**, 7774 (1987).
[27] R. Möller, U. Albrecht, J. Boneberg, B. Koslowski, P. Leiderer, and K. Dransfeld, J. Vac. Sci. Technol. B **9**, 506 (1991).
[28] O. Marti, H. Bielefeld, B. Hecht, S. Herminghaus, P. Leiderer, and J. Mlynek, Opt. Commun. **96**, 225 (1993).
[29] P. M. Adam, L. Salomon, F. de Fornel, and J. P. Goudonnet, Phys. Rev. B **48**, 2680 (1993).
[30] P. Dawson, F. de Fornel, and J-P. Goudonnet, Phys. Rev. Lett. **72**, 2927 (1994).
[31] P. Dawson, K. W. Smith, F. de Fornel, and J-P. Goudonnet, Ultramicroscopy **57**, 287 (1995).
[32] P. Dawson, B. A. F. Puygranier, W. Cao, and F. de Fornel, J. Microsc. **194**, pt. 2/3, 578 (1999).
[33] I. I. Smolyaninov, D. L. Mazzoni, and C. C. Davis, Phys. Rev. Lett. **77**, 3877 (1996).
[34] I. I. Smolyaninov, D. L. Mazzoni, J. Mait, and C. C. Davis, Phys. Rev. B **56**, 1601 (1997).
[35] S. I. Bozhevolnyi and V. Coello, Phys. Rev. B **58**, 10 899 (1998).
[36] S. I. Bozhevolnyi and F. A. Pudodin, Phys. Rev. Lett. **78**, 2823 (1997).
[37] S. I. Bozhevolnyi, B. Vohnsen, I. I. Smolyaninov, and A. V. Zayats, Opt. Commun. **117**, 417 (1995); S. I. Bozhevolnyi, I. I. Smolyaninov, and A. V. Zayats, Phys. Rev. B **51**, 17 916 (1995); S. I. Bozhevolnyi, *ibid.* **54**, 8177 (1996); S. I. Bozhevolnyi, V. A. Markel, V. Coello, W. Kim, and V. M. Shalaev, *ibid.* **58**, 11 441 (1998).
[38] D. P. Tsai, J. Kovacs, Z. Wang, M. Moskovits, V. M. Shalaev, J. S. Suh, and R. Botet, Phys. Rev. Lett. **72**, 4149 (1994).
[39] T. Klar, M. Perner, S. Grosse, G. von Plessen, W. Spirkl, and J. Feldman, Phys. Rev. Lett. **80**, 4249 (1998).
[40] J. R. Krenn, W. Gotschy, D. Somitsch, A. Leitner, and F. R. Aussenegg, Appl. Phys. A: Mater. Sci. Process. **61**, 541 (1995); J. R. Krenn, R. Wolf, A. Leitner, and F. R. Aussenegg, Opt. Commun. **137**, 46 (1997).
[41] J. R. Krenn, A. Dereux, J. C. Weeber, E. Bourillot, Y. Lacroute, J-P. Goudonnet, G. Schider, W. Gotschy, A. Leitner, F. R. Aussenegg, and C. Girard, Phys. Rev. Lett. **82**, 2590 (1999).
[42] B. A. F. Puygranier, Ph.D. thesis, Queen's University of Belfast, UK, 2001.
[43] R. Carmanati and J. J. Greffet, Opt. Commun. **116**, 316 (1995).
[44] J-C. Weeber, F. de Fornel, and J-P. Goudonnet, Opt. Commun. **126**, 285 (1996).
[45] A. Madrazo and M. Nieto-Vesperinas, J. Opt. Soc. Am. A **13**, 785 (1996).
[46] W. P. Chen, G. Ritchie, and E. Burstein, Phys. Rev. Lett. **37**, 993 (1976).
[47] H. Dohi, S. Tago, M. Fukui, and O. Tada, Solid State Commun. **55**, 1023 (1985).
[48] C. J. T. Rea, Ph.D. thesis, Queen's University of Belfast, U.K. 1997.
[49] P. B. Johnston and R. W. Christy, Phys. Rev. B **6**, 4370 (1972).
[50] U. Schröder, Surf. Sci. **102**, 118 (1981).
[51] G. P. Bryan-Brown, S. J. Elston, and J. R. Sambles, J. Mod. Opt. **38**, 1181 (1991).
[52] D. K. Burge, J. M. Bennett, R. L. Peck, and H. E. Bennett, Surf. Sci. **16**, 303 (1969); J. M. Bennett, J. L. Stanford, and E. J. Ashley, J. Opt. Soc. Am. **60**, 224 (1970).
[53] T. Tamai, IEEE Trans. Compon., Hybrids, Manuf. Technol. **12**, 43 (1989).
[54] P. W. Wilson, J. Vac. Sci. Technol. A **6**, 2386 (1988).
[55] H. Dlala, M. Amlouk, S. Belgacem, P. Girard, and D. Barjon, Eur. Phys. J.: Appl. Phys. **2**, 13 (1998).
[56] G. J. Kovacs, Surf. Sci. **78**, 245 (1978).
[57] N. Mehan and A. Mansingh, Appl. Opt. **39**, 5214 (2000).
[58] S. Russev, L. Vassilev, V. Vulchev, L. Lutov, and Tz. Argirov, J. Phys.: Condens. Matter **6**, 6237 (1994).
[59] R. J. Bell, R. W. Alexander, C. A. Ward, and I. L. Tyler, Surf. Sci. **48**, 253 (1975).
[60] M. P. Connolly and P. Dawson, J. Appl. Phys. **78**, 5522 (1995).
[61] L. Wendler and R. Haupt, Phys. Status Solidi B **143**, 131 (1987).
[62] D. Van Labeke, F. I. Baida, and J.-M. Vigoureux, Ultramicroscopy **71**, 351 (1998).
[63] F. I. Baida, D. Van Labeke, and J.-M. Vigoureux, Phys. Rev. B **60**, 7812 (1999).
[64] F. I. Baida, D. Van Labeke, and J.-M. Vigoureux, Opt. Commun. **171**, 317 (1999).